lubricants

MDPI

Article

Study on Secondary Remelting Modification of Laser Cladding Ni60/WC Composite Coatings

Jianwen Zhang [1], Gui Wang [1,2], Jingquan Wu [1,2], Jiang Huang [3], Wenqing Shi [4], Fenju An [1] and Xianglin Wu [1,2,*]

[1] School of Mechanical Engineering, Guangdong Ocean University, Zhanjiang 524088, China; zhangjw@gdou.edu.cn (J.Z.); 13828230363@163.com (G.W.); wujq@gdou.edu.cn (J.W.); afj1022@126.com (F.A.)
[2] Guangdong Engineering Technology Research Center of Ocean Equipment and Manufacturing, Zhanjiang 524088, China
[3] School of Electronics and Information Engineering, Guangdong Ocean University, Zhanjiang 524088, China; huangjiang@gdou.edu.cn
[4] School of Materials and Science and Engineering, Guangdong Ocean University, Yangjiang 529500, China; swqafj@163.com
* Correspondence: wuxiangl@gdou.edu.cn

Abstract: In this study, laser melting experiments of Ni60/WC composite powder coatings were carried out using a laser, and the surface morphology and microstructure of the coatings were analyzed using a scanning electron microscope (SEM) coupled with energy dispersive X-ray spectroscopy (EDS). In addition, hardness testing equipment was used to assess the hardness of the coatings and an electrochemical workstation was used to characterize their corrosion resistance. The key findings demonstrate substantial variations in coating performance based on remelting parameters. The coatings processed without secondary laser remelting exhibited an average hardness of 501.36 (standard deviation 154.46) $HV_{0.2}$, a self-corrosion potential of −0.039 V, and a self-corrosion current density of 8.11×10^{-4} A/cm^2. In contrast, some coatings were subjected to secondary remelting at 800 mm/min (S 800). The laser is used to scan the surface of the cladding with the laser on the surface of the cladding, and the speed is the feed rate of the laser scanning. XRD analysis revealed intensified main peaks, indicative of elevated solid solution and carbide content. SEM micrographs displayed fishbone-like and feather-like morphologies, with the hardness increasing to 622.98 (standard deviation 9.60) $HV_{0.2}$ and the corrosion metrics improving to −0.038 V and 2.86×10^{-5} A/cm^2. In contrast, coatings remelted at 600 mm/min (S600) exhibited broader but less intense XDR peaks, alongside diminished reticulation in SEM imagery. These samples demonstrated marginally lower hardness 599.91 (standard deviation 8.35) $HV_{0.2}$ but superior corrosion resistance, with a self-corrosion potential of −0.012 V and current density of 2.64×10^{-5} A/cm^2. The results underscore the critical influence of laser scanning velocity and remelting frequency on microstructural evolution, mechanical strength, and electrochemical stability. Enhanced hardness correlates with refined microstructural features, while enhanced corrosion resistance arises from reduced defect density and stabilized electrochemical activity.

Keywords: laser cladding; Ni60/WC; remelting; hardness

check for updates

Received: 7 April 2025
Revised: 29 April 2025
Accepted: 13 May 2025
Published: 15 May 2025

Citation: Zhang, J.; Wang, G.; Wu, J.; Huang, J.; Shi, W.; An, F.; Wu, X. Study on Secondary Remelting Modification of Laser Cladding Ni60/WC Composite Coatings. *Lubricants* **2025**, *13*, 222. https://doi.org/10.3390/lubricants13050222

Copyright: © 2025 by the authors. Licensee MDPI, Basel, Switzerland. This article is an open access article distributed under the terms and conditions of the Creative Commons Attribution (CC BY) license (https://creativecommons.org/licenses/by/4.0/).

1. Introduction

Laser cladding, as a cutting-edge surface modification technology, has gained prominence in critical industries such as aerospace, energy systems, and high-end machinery due to its ability to fabricate metallurgically bonded coatings with superior wear resistance, corrosion resistance, and thermal stability [1]. However, conventional laser-clad coatings

(e.g., Ni-based or Fe-based alloys) face inherent limitations under extreme operational conditions. For instance, their crystalline structures are prone to high-temperature softening and stress-induced crack propagation, which severely restrict service lifetimes in turbine blades or nuclear reactor components.

Chao Zeng et al. [2] successfully prepared a series of nickel-based coatings under different laser power conditions. With the help of the theory of continuous damage mechanics, the pore damage in the coating was clearly defined. The results of the study show that a strong metallurgical bond can be constructed between the substrate and the cladding coating by laser cladding technology. With the change in laser power, the severity of porosity did not show a monotonically changing trend and did not continue to intensify with the increase in laser power.

Chunlun Chen et al. [3] utilized Ni60 composite powder with nano and micron WC particles to prepare WC/Ni coatings by laser cladding on the surface of an impeller, and the results showed that the addition of WC particles enhanced the microhardness and wear resistance of the coatings.

Teng Wu et al. [4] fabricated a single-layer Fe/WC cladding and a dual-layer coating system (combining Fe/WC with a Ni60 transition layer) on 60Si2Mn spring steel. The experimental results revealed that the Ni60 interlayer minimized porosity and crack formation in the Fe/WC composite coating while promoting upward columnar crystal growth. Notably, the transition layer had no significant impact on the solidification behavior; both coatings exhibited dendritic structures with interdendritic eutectic phases. Mechanically, nickel diffusion slightly reduced the cladding's microhardness, and the Fe/WC composite coating showed higher average friction coefficients and wear volumes compared to the Ni60-enhanced variant. However, both coatings outperformed the base material in these properties.

In Xuelong, P et al. [5]'s study, composite coatings were prepared by fiber laser cladding of NiCrBSi alloy powder on the surface of Ti6AI4V substrate, and the coating dilution rate was similar at scanning speeds ranging from 5 mm/s to 15 mm/s, which was about 64.23%; at a scanning speed of 20 mm/s, the dilution rate was drastically reduced to 37.06%; and the average microhardness of the coatings was significantly increased to 1026.5 $HV_{0.2}$, with the other three coatings about 886.4 $HV_{0.2}$; and the lowest coefficient of friction of about 0.371 was obtained at a scanning speed of 20 mm/s, and was relatively stable with the lowest wear loss.

Laser cladding technology shows great potential in strengthening the surface properties of parts and preparing functional gradient materials. These studies provide an important theoretical and experimental basis for the application of Ni60/WC composite coatings. This paper compares the final processing results of single laser cladding and secondary remelting. Especially, it compares the macrostructure, microstructure, phase, hardness, and corrosion resistance of the workpiece. The results show that the workpiece with secondary remelting has better material properties.

Ni60 alloy is often used as a coating material for laser cladding because of its good wear resistance, corrosion resistance, and processability. And the addition of WC particles can further improve the hardness and wear resistance of the fusion cladding layer [6]. Studies have shown that laser cladding Ni60/WC composite coatings can significantly improve the service life of mechanical equipment [7], such as in the field of mining machinery, construction machinery, molds, and other fields, which shows good prospects for application.

Although laser cladding technology has many advantages, it still faces some challenges, such as the uneven organization of the cladding layer, high residual stress [8], easy to produce cracks, etc. These problems limit the further development and application

of laser cladding technology. Therefore, exploring new process methods to optimize the organization and properties of the cladding layer is the current research hotspot in the field of laser cladding [9].

As a widely utilized material in mechanical engineering, Q235 steel is recognized for its low carbon content, favorable weldability, and balanced mechanical characteristics. This research focuses on depositing Ni60/WC composite coatings onto Q235 substrates through laser cladding techniques, followed by surface enhancement via secondary laser irradiation to augment coating hardness and corrosion resistance. A key innovation involves precisely regulating secondary laser parameters to achieve microstructural refinement and decreased surface roughness in the clad layer, thereby optimizing its functional durability. The investigation systematically examines critical operational variables—including the laser energy input, beam traversal rate, and material deposition velocity—on the metallurgical structure and functional attributes of the coatings. Through parametric optimization, the study aims to develop high-performance surface layers with enhanced mechanical and anti-corrosive properties.

2. Materials and Methods

2.1. Experimental Materials

The experimental substrates consisted of Q235 carbon steel plates measuring 50 mm in length, 100 mm in width, and 3 mm in thickness. To ensure optimal adhesion and surface purity, substrate surfaces underwent progressive sanding using 400-grit followed by 800-grit abrasive paper, eliminating contaminants and oxide layers. The deposited coating material was formulated as a composite blend of 70% Ni60 alloy powder and 30% tungsten carbide (WC) particles, with the full chemical specifications detailed in Table 1. The range of Ni60 powder particle size is 40–109 μm, and the range of WC powder particle size is 28–153 μm.

Table 1. Ni60 powder and Q235 chemical composition (mass fraction, %).

Element	C	Cr	B	Mn	Si	Fe	P	S	Ni
Ni60	0.8–1.2	14–16	3–3.5	-	3.5–4.0	14–15	0.02	0.02	Bal
Q235	0.22	-	-	0.3–0.7	0.35	Bal	0.04	0.05	-

The experimental substrates used were Q235 carbon steel plates with dimensions of 50 mm × 100 mm × 3 mm (length × width × thickness). To ensure optimal adhesion and surface cleanliness, the substrates were sanded progressively with 400-grit and then 800-grit abrasive paper to remove surface contaminants and oxide layers.

The coating material was a composite consisting of 70% Ni60 alloy powder and 30% tungsten carbide (WC) particles. The particle size range of the Ni60 powder was 40–109 μm, while that of the WC powder was 28–153 μm. Detailed chemical compositions of the powders are provided in Table 1.

The laser cladding experiment uses an XL-F2000T (Shenzhen Xinglai Laser Technology Co., Ltd., Shenzhen, China) laser cladding system, which has high energy density and stable beam quality and is suitable for the surface modification of metal materials. During the cladding process, the laser power and scanning speed are adjusted to ensure the formation of a good metallurgical bond between the cladding layer and the base material.

Laser cladding was performed using an XL-F2000T system (Shenzhen Xinglai Laser Technology Co., Ltd.), which features a high energy density and stable beam quality, making it suitable for the surface modification of metallic materials. During the cladding process,

laser power and scanning speed were carefully controlled to ensure the formation of a good metallurgical bond between the cladding layer and the substrate.

The samples were cut into 10 × 10 mm and 15 × 15 mm sizes for subsequent experiments using an AR40-MA medium-wire cutting machine manufactured by Beijing Anderson Jianqi Digital Equipment Co., Beijing, China.

Post-cladding, the samples were cut into sizes of 10 mm × 10 mm and 15 mm × 15 mm using an AR40-MA medium-wire cutting machine (Beijing Anderson Jianqi Digital Equipment Co.).

The microstructure of the cladding was characterized by a Hitachi TM4000Plus scanning electron microscope (SEM) manufactured by Hitachi High-Technologie, Osaka, Japan, which can provide high-resolution surface morphology and microstructure information, and combined with energy dispersive X-ray spectrometry (EDS), it can qualitatively and quantitatively analyze the distribution of the elements in the coatings, so as to study the compositional homogeneity and phase composition of the coatings.

The microstructure of the coatings was characterized using a Hitachi TM4000Plus scanning electron microscope (SEM) from Hitachi High-Technologies, Osaka, Japan. Combined with energy-dispersive X-ray spectrometry (EDS), this allowed for qualitative and quantitative analysis of element distribution and phase composition in the coatings.

The hardness test of the coating was performed with the MHV D-1000AT hardness test equipment produced by Shanghai Multi-crystal Precision Instrument Manufacturing Co., Shanghai, China. During the test, the applied load was set at 1.96 N and the loading time was 10 s. In order to comprehensively evaluate the hardness distribution of the coating, 9 points were tested from the surface of the fused cladding to the substrate along the longitudinal direction with a test spacing of 0.1 mm; meanwhile, 2 points were tested on the left and right sides of the substrate transversely with a spacing of 0.1 mm. This test method can effectively reflect the hardness gradient change between the coating and the substrate.

Hardness testing was conducted using an MHV D-1000AT microhardness tester (Shanghai Multi-crystal Precision Instrument Manufacturing Co.) with a load of 1.96 N and a dwell time of 10 s. To evaluate the hardness gradient across the coating and substrate, nine points were measured longitudinally at 0.1 mm intervals from the surface of the cladding to the substrate. Additionally, two points were measured transversely on each side of the substrate at a 0.1 mm spacing. This test method can effectively reflect the hardness gradient change between the coating and the substrate.

The physical phase of the coating was analyzed using an XRD-6100 X-ray diffractometer (XRD) from Shimadzu, Tokyo, Japan. The diffraction scanning range was from 10 to 80 degrees with a scanning step of 0.04 degrees and a scanning speed of 6°/min [10]. The XRD analysis can determine the physical phase composition in the coating and reveal the phase transformation law and strengthening mechanism of the Ni60/WC composite coating.

Phase composition was analyzed using an XRD-6100 X-ray diffractometer (Shimadzu, Tokyo, Japan) with a scanning range of 10–80°, a step size of 0.04°, and a scanning speed of 6°/min [10]. This analysis provided insight into phase transformations and the strengthening mechanism of the Ni60/WC composite coatings.

The corrosion resistance test of the coatings was performed using a CS Studio electrochemical workstation from Wuhan Corette Instrument Co. in China. Considering that the main component of a seawater environment is NaCl, the corrosive medium was set as NaCl solution with a mass fraction of 3.5%. The tests were performed using a three-electrode electrochemical cell system, in which the coating sample was used as the working electrode, the platinum sheet as the auxiliary electrode, and the saturated calomel electrode (SCE) as the reference electrode. The scanning rate of the electrochemical tests was set at

0.5 mV/s and the sampling frequency was 1 Hz. The corrosion resistance of the coatings in the simulated seawater environment could be evaluated by kinetic potential polarization curves.

Corrosion resistance tests were performed with a CS Studio electrochemical workstation (Wuhan Corette Instrument Co., Wuhan, China). A 3.5 wt.% NaCl solution was used to simulate a seawater environment. The test setup included a three-electrode electrochemical cell: the coated sample as the working electrode, a platinum sheet as the auxiliary electrode, and a saturated calomel electrode (SCE) as the reference electrode. The polarization tests were carried out at a scan rate of 0.5 mV/s with a sampling frequency of 1 Hz. The corrosion behavior of the coatings was evaluated via potentiodynamic polarization curves.

2.2. Experimental Method

In the laser cladding experiments, we used the pre-positioned powder method to spread the Ni60/WC composite powder uniformly on the surface of the Q235 steel substrate. Subsequently, the fused cladding layer was formed using laser beam scanning with a power of 1200 W and a speed of 800 mm/min, as well as a defocusing amount of 3 mm and a spacing of 1.2 mm. In order to further optimize the process parameters, different scanning speeds (800 mm/min and 600 mm/min, respectively) were designed to investigate their effects on the morphology, microstructure, and properties of the fused cladding layer. After the completion of the fusion cladding process, the samples were cut, sanded, and polished, and metallographic specimens were prepared for subsequent microstructural observation and performance testing.

The laser cladding process employed the pre-placed powder method, where the Ni60/WC composite powder was uniformly distributed on the surface of the Q235 steel substrates. Cladding was performed using a laser power of 1200 W, a scanning speed of 800 mm/min, a defocus distance of 3 mm, and a scanning line spacing of 1.2 mm.

To assess the influence of scanning speed on the cladding quality, an additional speed of 600 mm/min was tested. After laser processing, the samples were sectioned, sanded, and polished to prepare metallographic specimens for further microstructural analysis and performance evaluation.

The optimal process conditions were determined by comparing the hardness, microstructure, and corrosion resistance of the fused cladding layer under different process parameters. At the same time, combined with the SEM, EDS, and XRD analysis results, the strengthening mechanism and corrosion resistance mechanism of Ni60/WC composite coatings were explored to provide theoretical basis for the further application of laser cladding technology.

The optimal processing parameters were determined by comparing hardness, microstructure, and corrosion resistance under different conditions. SEM, EDS, and XRD analyses were also used to investigate the strengthening and corrosion resistance mechanisms of the Ni60/WC composite coatings, aiming to provide a theoretical basis for further applications of laser cladding technology.

3. Results and Discussion

3.1. Macrogram

In the cladding without remelting (Figure 1a), the surface is characterized by clearly visible fusion lines between the cladding channels, which indicate the bonding of the individual channels and the transition characteristics in the heat-affected zone.

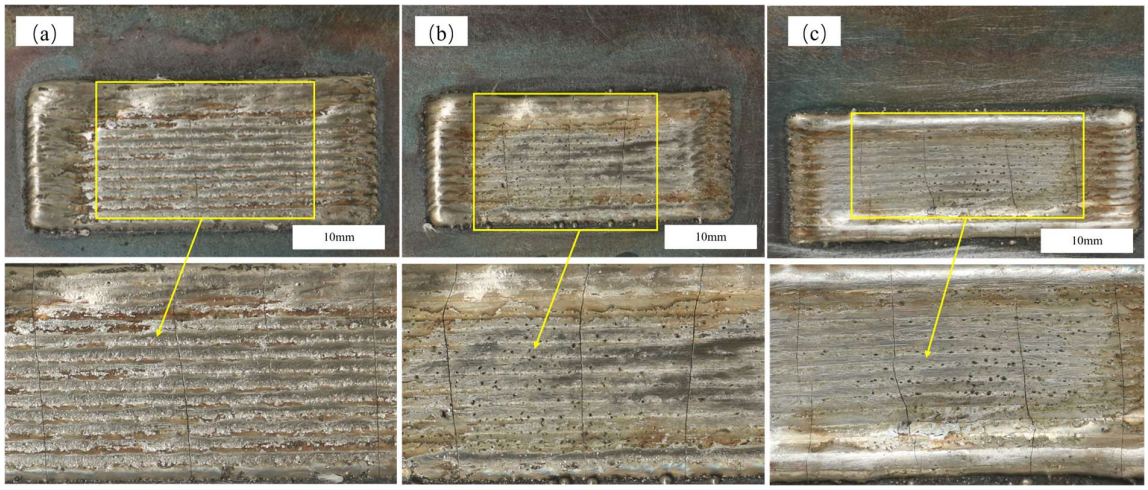


Figure 1. Fused cladding layers with different remelting speeds. (**a**) Single cladding [10] (**b**) Remelting speed S 600 mm/min (**c**). Remelting speed S 800 mm/min.

When the remelting speed was set to 600 mm/min (Figure 1b), the surface of the fused cladding layer showed a distinctive concave feature compared to the un-remelted cladding layer, with the central part being more concave and the peripheral part appearing more prominent. This morphological change may be related to the uneven heat distribution during the remelting process and the difference in cooling rate. Under this condition, the presence of three tiny cracks was observed on the surface, which may have originated from the accumulation of internal stresses in the material during the curing process, reflecting the vulnerability of this melted cladding during stress release [11–13].

When the remelting speed was further increased to 800 mm/min (Figure 1c), the surface characteristics changed again. At this time, the fused cladding still maintains the morphology of concave in the center and protruding in the periphery, but the number of cracks increased significantly to four. This phenomenon suggests that at higher remelting speeds, the cooling rate of the cladding layer is accelerated, which may lead to more pronounced stress concentration and structural instability, resulting in an increase in the number of cracks. The microstructural and mechanical properties in this case need to be further investigated to reveal the mechanism leading to crack propagation.

Remelting treatment has a significant effect on the morphology of the cladding layer and its crack characteristics, and different remelting rates are directly related to the stress distribution and its stability in the cladding layer. This provides an important reference for further research on the optimization of the properties of cladding materials.

3.2. Physical Phase Analysis

This can be seen through Figure 2, in the Ni60/WC composite powders used in the laser cladding process, the fused cladding layer without remelting treatment mainly contains four phases: the γ-(Fe, Ni) phase, $M_{23}C_6$ phase, Cr_3C_2 phase, and Fe_5C_2 phase [14–16]. The presence of these phases jointly affects the microstructure of the cladding and its mechanical properties.

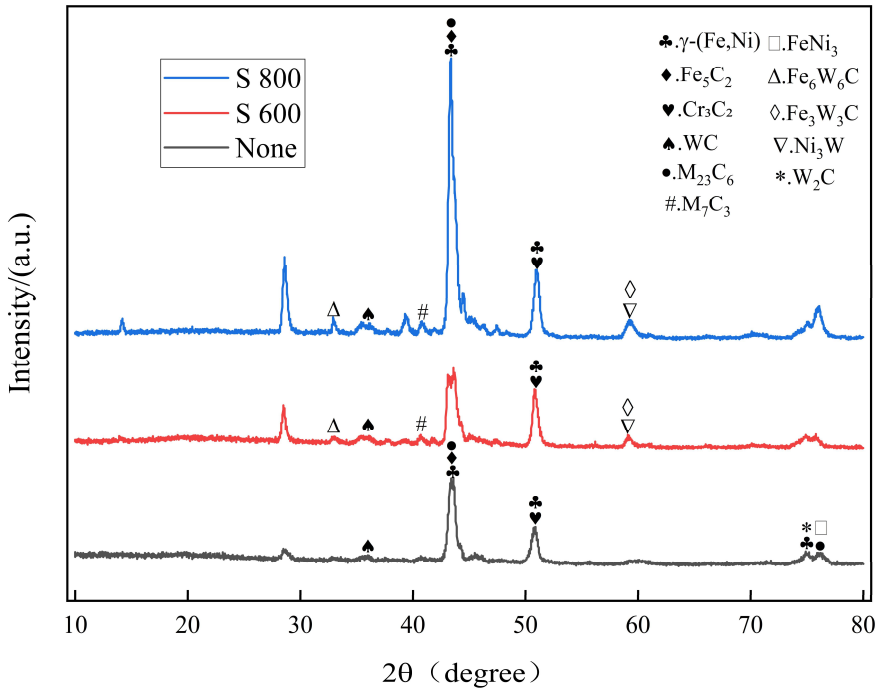


Figure 2. XRD pattern analysis.

When the remelting speed was set to 800 mm/min, the γ-(Fe, Ni) solid solution and carbide phases such as $M_{23}C_6$ in the fused cladding layer increased significantly, and the main diffraction peak was shifted slightly to the right, which may be related to the stress concentration. At this time, new diffraction peaks corresponding to the crystal structures of the Fe_6W_6C and Fe_3W_3C phases appeared in the X-ray diffraction (XRD) spectra. This change indicates that at this remelting rate, the chemical composition and phase structure of the alloy have evolved significantly to form new stabilized phases. Meanwhile, the diffraction peak width of WC increased, which is related to the change in crystal defect density and interaction [17]. The intensity of the characteristic diffraction peaks of $FeNi_3$ was enhanced, indicating that the formation and stabilization of the $FeNi_3$ phase were enhanced during the laser remelting process [18], which contributed to the improvement of the overall properties of the fused cladding. In comparison, when the remelting speed was reduced to 600 mm/min, the main peaks of the γ-(Fe, Ni), $M_{23}C_6$, and Fe_5C_2 phases in the fused cladding layer showed significant broadening, a reduction in grain size to 8.6 nm, and weakening in intensity. This phenomenon indicates a significant change in the crystal structure, which is manifested in the reduction in grain size. This grain refinement phenomenon usually results in an increased number of grain boundaries, which triggers the broadening of the XRD peaks. In addition, grain refinement is often accompanied by an increase in microscopic strain, which further exacerbates the broadening.

When the scanning speed was increased from 600 mm/min to 800 mm/min, the carbide grain size increased from 8.6 nm to 11.4 nm, while the hardness increased from 599.91 $HV_{0.2}$ to 622.98 $HV_{0.2}$. This anomaly is due to the competition between ultrafast solidification kinetics and multi-scale strengthening mechanisms at high scanning speeds, as follows: Ashby–Orowan precipitation enhancement dominates (critical size effect of nanocarbide density increase); there is enhanced solute retention and solution enhancement; thermal stress-induced dislocation density proliferation occurs; and Hall–Petch weakening is overridden by the above mechanism. The increase in the standard deviation of hardness (8.35→9.60) reveals the gradient distribution characteristics of the micromechanical properties in the melt pool, which needs to be further optimized by the process of homogenization.

3.3. Micrograph Analysis

The microstructure of the fused cladding layers with different remelting speeds and the results of elemental compositional analysis are listed in Table 2. In Figure 3a, the compositional analysis of the white irregular tetragonal particles shown in Spectrum A shows that the atomic ratio of element C is 8.89 and that of element W is 9.66. These atomic ratios are close to 1:1, suggesting that these white particles are most likely ruptured WC particles. The rupture in the WC particles may be related to the high temperature, rapid cooling, and stress state of the material in the laser fusion cladding process, which leads to the brittle breakage of the structure [19].

Table 2. Distribution of major elements at EDS scanning sites.

Element		C	Cr	Fe	Ni	W
Spectrum A	Weight %	1.80	12.64	23.63	27.45	29.93
	Atomic %	8.89	14.42	25.10	27.75	9.66
Spectrum B	Weight %	1.71	11.54	27.55	30.81	27.19
	Atomic %	2.45	14.18	31.53	33.54	9.45
Spectrum C	Weight %	0.42	11.43	19.62	20.73	45.32
	Atomic %	2.69	16.87	26.97	27.12	18.93
Spectrum D	Weight %	1.03	14.39	40.01	19.58	23.18
	Atomic %	5.19	16.77	43.43	20.22	7.64

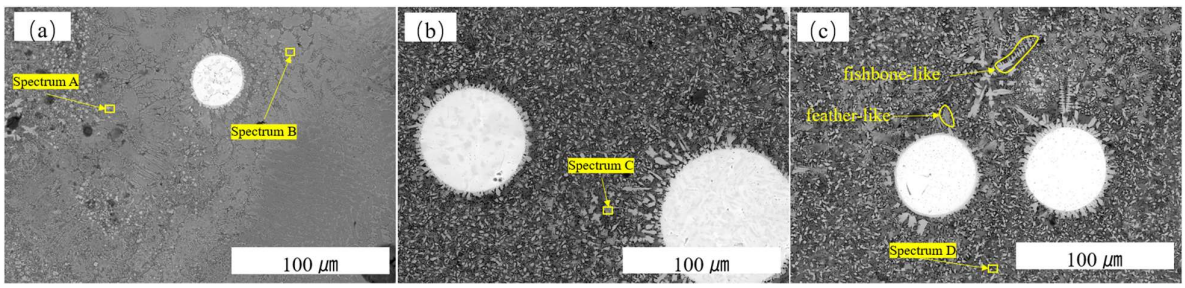


Figure 3. Microstructure and EDS analysis of the fused cladding layer with different remelting speeds. (**a**) Electron micrograph of the fused cladding layer without secondary laser scanning. (**b**) Electron micrograph of the fused cladding layer scanned at remelting speed S 600 mm/min. (**c**) Electron micrograph of the fused cladding layer scanned at remelting speed S 800 mm/min.

The compositions of each microzone of the Ni60/WC fused cladding layer at different remelting speeds were further analyzed by an energy dispersive spectroscopy (EDS) analyzer, and the results of Spectrum B showed that the content of elemental C was 2.45%, the content of elemental Ni was 30.81%, and the content of elemental Fe was 27.55%. Based on these compositional data, it can be hypothesized that the matrix of this microzone is mainly γ-(Fe, Ni) solid solution, and the formation of the corresponding metal matrix may provide certain toughness and plasticity for the cladding process.

Spectrum C in Figure 3b generates a small reticulated organization with 0.42% of elemental C, 11.43% of elemental Cr, and a decrease in the content of elemental Ni to 20.73%, whereas the content of elemental Fe is 19.62%. The secondary sweep of the laser speed of 600 mm/min prolongs the existence of the molten pool, and the heat input increases, and the WC particles are further dissolved, and the released C with the Cr, Fe, etc., in the matrix forms fine M_7C_3 or $M_{23}C_6$ carbides [20], rather than coarse $M_{23}C_6$. These carbides precipitated along the grain boundaries or dendrites, forming a diffused distribution of a fine mesh structure. By enabling the uniform precipitation of carbides in the matrix, the carbides are diffusely distributed, destroying the original reticulation to

reduce the reticulation in the SEM. Slower cooling allows some of the γ-(Fe, Ni) austenite to transform into martensite or bainite during cooling, further reducing the residual austenite content, which is shown in Figure 2 as a weakening of the XRD peak intensity.

In the observation of microstructure, the Spectrum D microzone composition analysis in Figure 3c indicates that the chemical composition of the fused cladding layer with a remelting rate of 800 mm/min shows an increase in the content of elements such as Cr and Fe and a decrease in the Ni element, as compared to that of the un-remelted fused cladding layer. The significant increase in these elements indicates that more eutectic carbides are formed during the solidification process, which means that the hardness and wear resistance of the cladding layer are expected to be effectively improved at high remelting speeds compared with the cladding layer without remelting treatment [21]. The generation of eutectic carbides not only improves the wear resistance of the material, but also potentially provides the cladding with superior mechanical and corrosion resistance properties.

The high scanning speed (800 mm/min) results in low heat input and the very fast cooling rate of the melt pool, and the carbon (C) and alloying elements (e.g., Cr, W) generated by the decomposition of WC cannot diffuse sufficiently, resulting in the formation of a fishbone (ledeburite) or feathery (martensite/bainite) non-equilibrium organization. The fishbone structure resembles the rapidly solidifying organization of eutectic brinellite (alternating growth of γ-phase and carbides). Feathery structures have some areas where austenite is directly transformed to lath martensite or bainite as the cooling rate exceeds a critical value.

Rapid cooling inhibits the transformation of austenite to martensite, resulting in high residual austenite γ-(Fe, Ni) content and the significant enhancement of the main peak of the γ-phase in the XRD. The $M_{23}C_6$ carbides are coarsened, and some of the undissolved $M_{23}C_6$ carbides are aggregated in the rapid solidification, with a simultaneous enhancement in the intensity of the diffraction peaks [10]. The mixed organization of coarser carbides and residual austenite leads to large fluctuations in hardness, but the local hardness is significantly enhanced if martensite is present.

The non-equilibrium solidification (Riesling) and the austenite–martensite phase transition at a very fast cooling rate of 800 mm/min led to the alternate distribution of coarse carbides and hard/soft phases. Moreover, 600 mm/min high heat input promotes the dissolution–reprecipitation of carbides and the formation of dispersed, fine-grained carbides, which disrupts the continuous reticulation morphology.

Figure 4a–c show the scanning electron microscope (SEM) microstructure profiles of the surface of the fused cladding layer at different remelting speeds. The statistical results of the particle size distribution shown in Figure 4d–f show that the distribution curves after Gaussian fitting exhibit typical normal distribution characteristics (R^2 is 0.91, 0.93, and 0.98, respectively). Combined with the EDS spectroscopic analysis data in Figure 3 and Table 2, it was confirmed that the white irregular tetragonal/polygonal particles were mainly WC hard phases. In the pristine fused cladding layer without remelting treatment (Figure 4a), the WC particles showed typical unmelted characteristics, with an average equivalent diameter of 2.24 μm and a size distribution in the range of 0.61–3.92 μm. When a remelting speed of 600 mm/min (S600) was used (Figure 4b), the WC particles underwent a significant refinement to form sizes of about 0.44–2.75 μm, with the average equivalent diameter decreasing to 1.21 μm. The diameter decreased to 1.21 μm, which is 46.9% smaller than the particle size in the un-remelted fused cladding. It is noteworthy that the particle size distribution at this speed shows an obvious single-peak feature with a standard deviation of 0.42 μm, indicating that the remelting process has a significant effect on the fragmentation and dispersion of WC particles. Compared with

S600, the remelting treatment with a higher scanning speed S800 (Figure 4c) increased the average particle size to 1.41 μm, which is 0.20 μm. Further mechanistic analyses showed that the remelting parameters modulate the behavior of WC particles by influencing the thermal cycling characteristics of the melt pool. Under S 600 conditions, the higher energy density led to the prolonged presence of the melt pool, which promoted the decomposition of WC particles. The results of this study provide an experimental basis for the microstructure modulation of laser-melted WC-reinforced metal matrix composites, and the particle refinement effect is optimal under the S 600 parameter, which can effectively enhance the hardness of the material and thus improve the wear resistance [22,23].

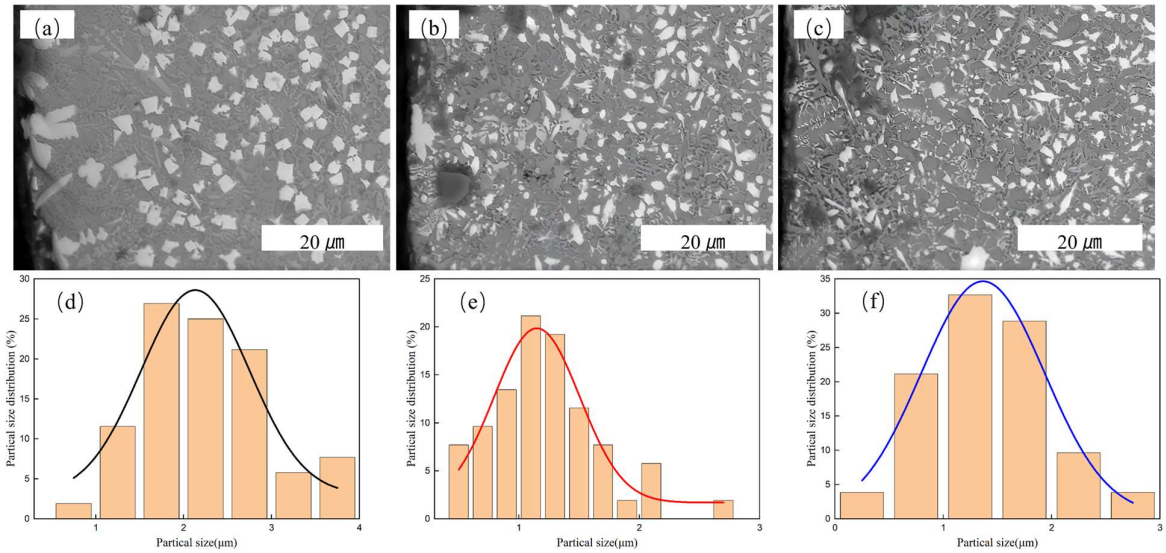


Figure 4. Scanning electron micrographs of the upper layer of the fused cladding surface with different remelting speeds. (**a**) 1500× electron microscope image of the fused cladding layer without secondary laser scanning. (**b**) 1500× electron microscope image of the fused cladding layer scanned at remelting speed S 600 mm/min. (**c**) 1500× electron microscope image of the fused cladding layer scanned at remelting speed S 800 mm/min. (**d**) No secondary remelting to break particle distribution. (**e**) Distribution of broken particles at 600 mm/min secondary remelting rate. (**f**) Distribution of broken particles at 800 mm/min secondary remelting rate.

Analysis of the Tafel curves in Figure 5 and Table 3 shows that the organizational inhomogeneity and defects of the unsecondary remelted layer resulted in the worst corrosion performance (the most negative self-corrosion potential and the highest self-corrosion current density) [24]. During the 800 mm/min secondary sweep rapid cooling, the self-corrosion potential Ecorr was slightly positively shifted. The 600 mm/min secondary scanning of the fused cladding layer significantly improved the corrosion resistance (self-corrosion potential was positively shifted and the self-corrosion current density was 2.86×10^{-5} A.cm^{-2}) [24]. By optimizing the secondary scanning speed, a synergistic improvement in the corrosion resistance and mechanical properties can be achieved.

Table 3. Experimental results of corrosion in NaCl medium.

Sample	None	S 600	S 800
E_{corr}/V	−0.039	−0.012	−0.038
I_{corr}/(A.cm^{-2})	8.11×10^{-4}	2.86×10^{-5}	2.64×10^{-5}

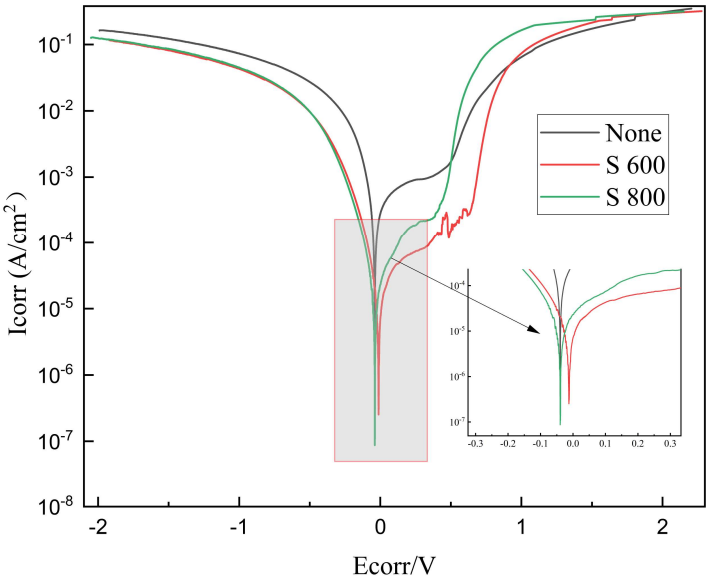


Figure 5. Polarization curves of molten cladding layers with different remelting speeds.

The 'automatic fitting Tafel slope' function of CorrTest. CSStudio software (https://www.controlsystemstudio.org/) was used to obtain the Tafel slopes of the anode and cathode branches. For the goodness of fit analysis, the original polarization data (η and log |i|) are derived from the software, and the linear regression is performed again to calculate the coefficient of determination (R^2). The results show that the Tafel slope anode R^2 = 0.99, the Tafel slope cathode R^2 = 0.99; the Tafel slope anode R^2 of the S 600 sample is 0.95, and the Tafel slope cathode R^2 is 0.96. The Tafel slope anode R^2 of the S 800 sample is 0.98, and the Tafel slope cathode R^2 is 0.99. It shows that the fitting quality is reliable.

The self-corrosion current density of the unsecondarily remelted coatings, 8.11×10^{-4} A.cm^{-2}, indicated a high corrosion rate, which mainly originated from localized corrosion channels due to coating defects (pores, unfused particles) [23]. The fast cooling rate of the coating without secondary remelting results in an inhomogeneous organization including coarse carbides (e.g., $M_{23}C_6$), residual austenite (γ-(Fe, Ni)), and unfused WC particles. This inhomogeneity tends to form localized galvanic coupling corrosion and accelerates the corrosion rate. The presence of pores, cracks, and other defects in the unfused layer provides diffusion channels for corrosive media (e.g., Cl^-) [25,26], which further aggravates corrosion. The interface between the coarse carbide and the matrix and the residual austenite region are corrosion-sensitive areas, resulting in a high current density.

Rapid cooling at 800 mm/min secondary scanning creates a non-equilibrium organization with limited improvement in corrosion performance due to residual austenite and coarse carbides. Rapid cooling leads to non-equilibrium solidification and the formation of fishbone and feathery (martensite/bainite) structures, which are corrosion sensitive, and the γ-(Fe, Ni) austenite in the fishbone structure is susceptible to selective dissolution in the corrosive medium. The carbide distribution is uneven, and the interface between the coarse $M_{23}C_6$ carbide and the matrix is a corrosion-preferred region. Although the organization is still not uniform, the secondary remelting reduces the pores and unmelted particles, and the corrosion current density is significantly reduced by an order of magnitude compared to the un-remelted layer.

The low scanning speed (600 mm/min) increases the heat input, which promotes the full decomposition of WC and diffusion of carbon elements to form fine and uniformly

distributed carbides (e.g., M_7C_3). In Figure 3, a reduction in the reticulation structure can be seen, indicating a more uniform distribution of carbides.

Fine grain strengthening and passivation ability enhance the fine carbide and ultra-fine grain matrix to reduce the tendency of local galvanic coupling corrosion. The homogeneous organization facilitates the formation of dense passivation film (Cr_2O_3), which significantly improves the corrosion resistance, and the uniform passivation film and fine grain organization inhibit the corrosion.

The S 600 sample exhibits better corrosion resistance than S800. In the fishbone-like/feather-like structure induced by rapid cooling, γ-(Fe, Ni) austenite becomes the active anode for microcouple corrosion due to its high Ni content and significant potential difference with martensite/carbides, resulting in selective dissolution. Its corrosion susceptibility is due to the following: a high Cr/Ni gradient at the austenite–matrix interface; a local current density surge driven by microcouples; and the synergistic damage of hydrogen embrittlement and pitting corrosion.

The secondary scanning speed affects the carbide distribution, grain size, and phase composition by regulating the heat input and cooling rate, which ultimately determines the passivation film stability and local corrosion tendency. The low speed (600 mm/min) optimizes the balance between thermodynamics (diffusion uniformity) and kinetics (passivation rate), which is the best choice for both corrosion resistance and mechanical properties.

In the field of material surface modification and coating performance research, the microstructure and performance characteristics of the coating are closely related to the processing parameters. As seen in Figure 6, the cross-sectional hardness distribution of the cladding layer with different remelting speeds shows that the hardness of the cladding layer without secondary remelting is low with a large standard deviation [10,27], and after the secondary scanning, the hardness is increased and the standard deviation is significantly reduced for both S 800 and S 600.

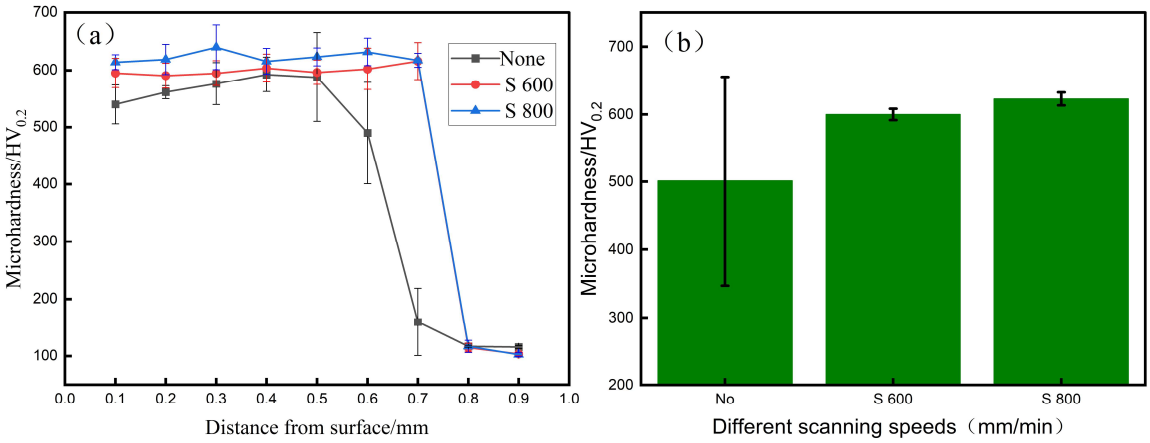


Figure 6. Cross-sectional hardness of fused cladding layers with different remelting speeds. (**a**) Cross-sectional hardness distribution of cladding layer. (**b**) Average hardness of cladding layer after scanning with different remelting speeds.

Through Figure 6a, showing the cladding layer cross-sectional hardness distribution, and Figure 6b, the average hardness is further analyzed. It can be seen that the coating without secondary remelting yields hardness measurements of 501.36 $HV_{0.2}$ and a standard deviation of 154.46, showing a large range of hardness fluctuations. This phenomenon implies a complex solidification and organization evolution mechanism. The microstructure and properties of the unsecondary remelted coatings may be caused by the rapid cooling leading to the uneven organization; during the initial melting process, the γ-(Fe, Ni) austenite in the molten pool could not follow the equilibrium solidification path for the

transformation due to the extremely fast cooling rate, but was retained by the rapid freezing. At the same time, the WC phase decomposes at high temperatures [28], but the carbides (e.g., $M_{23}C_6$, M_6C) produced by its decomposition cannot be uniformly distributed in the coating matrix due to the severe lack of time required for atomic diffusion, which results in a coarse and extremely unevenly distributed morphology. Within the microscopic regions of the coating, hard carbide-rich regions alternate with soft austenite regions, and this significant organizational heterogeneity is the root cause of the large fluctuations in the hardness of the coating (manifested as high standard deviations). Defects such as unmolten particles and pores may also be present in the unmolten layer. The presence of these defects acts as a weak point in the microstructure, which not only disrupts the continuity of the coating but also triggers stress concentrations within the coating [29]. When load is applied externally, the stress concentration area is prone to becoming the source of cracks, further aggravating the fluctuation of coating performance and seriously affecting the reliability of the coating in the actual service environment.

Regarding the coating characteristics of the second scanning speed of 600 mm/min, the hardness of the coating under this condition is 599.91 $HV_{0.2}$, and the standard deviation is only 8.35, which reflects a higher average value of hardness and good hardness uniformity. This is mainly attributed to the fact that the low scanning speed (600 mm/min) significantly extends the melt pool existence time [30]. The prolonged melt pool existence time implies an increase in heat input, and under the high temperature environment, WC can decompose sufficiently, and the carbon generated from the decomposition can diffuse sufficiently in the coating matrix and react chemically with the matrix, eventually forming fine and uniformly distributed $M_{23}C_6$ or M_7C_3 carbides. From the means of material microstructure analysis, the phenomenon of peak broadening in the XRD pattern indicates that the coating grains were refined, while the weakening of peak intensity implies that some carbides were dissolved, and these microstructural changes indicate that the organization was effectively refined. In addition, the slower cooling rate allows some of the γ-(Fe, Ni) austenite to undergo transformation to form hard phases (e.g., martensite or carbides), while the amount of residual austenite is reduced. In this process, the diffuse strengthening mechanism of fine carbides becomes dominant, effectively increasing the hardness of the coating while significantly improving the organization uniformity, resulting in a lower standard deviation of hardness. The high heat input during the second scan (600 mm/min) promotes atomic diffusion and the uniform precipitation of carbides. During this process, the hardness enhancement of the coatings mainly relies on the diffuse strengthening of the fine-grained carbides and the strengthening of the martensitic phase formed by partial austenite transformation. This reinforcing mechanism enables the coating to obtain high hardness and good organization uniformity at the same time.

At the second scanning speed of the 800 mm/min coating, the hardness of the coating was enhanced to 622.98 $HV_{0.2}$, with a standard deviation of 9.60 at this condition. The 24% enhancement compared with the un-remelted layer may be attributed to the rapid cooling process, where the cooling rate may exceed the critical cooling rate for austenite stabilization, which induces the partial transformation of γ-(Fe, Ni) to martensite and enhances the hardness and homogeneity of the coating.

In practical engineering applications, the existence of the un-remelted layer often becomes a shortcoming of the overall performance of the coating, reduces the protective effect of the coating on the substrate material, and restricts the service life of the coating in harsh service environments. Through the analysis of different secondary scanning speeds and the microstructure and properties of the un-remelted coatings, it can be seen that the secondary scanning process can significantly improve the organization and properties

of the coatings, and the different scanning speeds correspond to different strengthening mechanisms and performance.

4. Conclusions

(1) In the process of laser cladding Ni60/WC composite powder coatings, the precise control of the scanning speed can effectively promote the transformation of the coating microstructure, i.e., from the initial "non-equilibrium high defective organization" to the "homogeneous fine-grained reinforced organization". This mechanism can be attributed to the significant influence of the scanning speed on the thermal state of the melt pool and the solidification process.

(2) When the secondary remelting speed is set to 600 mm/min, the thermodynamic processes (e.g., solute diffusion uniformity) and kinetic processes (e.g., crystal growth rate) within the coating reach a more ideal equilibrium. Under these conditions, the corrosion resistance of the fusion-coated layer is significantly improved, which is shown by the positive shift in the self-corrosion potential and the reduction in the self-corrosion current density to 2.86 $\times$ 10^{-5} A·cm^{-2}, which indicates that the anodic dissolution process of the coating in the corrosive medium is effectively suppressed by this process parameter. This indicates that the anodic dissolution process of the coating in the corrosive medium is effectively suppressed under this process parameter, thus enhancing the corrosion resistance of the coating.

(3) After the second scanning treatment, the hardness of the coatings showed a tendency to increase and the standard deviation of the hardness data was significantly reduced, regardless of whether the scanning speed was 800 mm/min or 600 mm/min. Among them, when the scanning speed is S 600, the average value of coating hardness is 599.91 $HV_{0.2}$, which is 3.7% lower than the hardness value under the condition of S 800; however, the standard deviation is only 8.35, which means that the coating hardness is a little lower under the scanning speed of S 600, but the uniformity of the hardness distribution is more excellent. This variation rule of hardness and uniformity provides an important quantitative basis for optimizing the coating preparation process in practical engineering applications, and helps to achieve the goal of improving the comprehensive performance of the coating.

Author Contributions: Conceptualization, W.S., G.W., and J.H.; methodology, J.W.; software, X.W.; validation, J.H., X.W. and W.S.; formal analysis, X.W. and J.Z.; investigation, X.W. and J.Z.; resources, W.S., G.W. and J.H.; data curation, J.W.; writing—original draft preparation, X.W.; writing—review and editing, X.W., J.H. and J.Z.; visualization, J.W.; supervision, F.A. and J.Z.; project administration, W.S.; funding acquisition, J.W. and J.Z. All authors have read and agreed to the published version of the manuscript.

Funding: Supported by the National Natural Science Foundation Project (No. 62073089), the Zhanjiang Science and Technology Plan Project (No. 2021A05171), and the Laser Processing Team Project of Guangdong Ocean University (No. CCTD201823).

Data Availability Statement: Data are contained within the article.

Conflicts of Interest: The authors declare no conflicts of interest.

References

1. Findik, F. Laser cladding and applications. *Sustain. Eng. Innov.* **2023**, *5*, 1–14. [CrossRef]
2. Zeng, C.; Tian, W.; Liao, W.H.; Hua, L. Microstructure and porosity evaluation in laser-cladding deposited Ni-based coatings. *Surf. Coat. Technol.* **2016**, *294*, 122–130. [CrossRef]
3. Chen, C.; Feng, A.; Wei, Y.; Wang, Y.; Pan, X.; Song, X. Effects of WC particles on microstructure and wear behavior of laser cladding Ni60 composite coatings. *Opt. Laser Technol.* **2023**, *163*, 109425. [CrossRef]

4. Wu, T.; Shi, W.; Xie, L.; Gong, M.; Huang, J.; Xie, Y.; He, K. Study on the effect of Ni60 transition coating on microstructure and mechanical properties of Fe/WC composite coating by laser cladding. *Opt. Laser Technol.* **2023**, *163*, 109387. [CrossRef]
5. Ping, X.; Fu, H.; Sun, S.; Lin, J.; Lei, Y.; Wu, W.; Zhou, J. Effect of Nb addition on microstructure and properties of laser cladding NiCrBSi coatings. *Trans. IMF* **2018**, *96*, 304–312.
6. Zhao, J.; Li, R.; Feng, A.; Feng, H. Effect of rare earth La_2O_3 particles on structure and properties of laser cladding WC-Ni60 composite coatings. *Surf. Coat. Technol.* **2024**, *479*, 130569. [CrossRef]
7. Weng, F.; Yu, H.; Chen, C.; Liu, J.; Zhao, L.; Dai, J.; Zhao, Z. Effect of process parameters on the microstructure evolution and wear property of the laser cladding coatings on Ti-6Al-4V alloy. *J. Alloys Compd.* **2017**, *692*, 989–996. [CrossRef]
8. Zhao, C.; Yang, J.; Li, M.; Zhao, Q.; Ma, H.; Jia, X.; Zhang, H. Advances in surface laser cladding remanufacturing of shaft parts. *Manuf. Technol.* **2023**, *23*, 564–578. [CrossRef]
9. Wang, H.; Liu, X.H.; Han, B.; Lin, J.Y.; Han, X.R. Effects of Process Parameters on the Structure and Hardness of Components in Laser Direct Metal Forming. *IOP Conf. Ser. Mater. Sci. Eng.* **2019**, *631*, 022028. [CrossRef]
10. Wu, X.; Chen, J.; Huang, J.; Shi, W.; Wang, Q.; An, F.; Wu, J. Laser-Melted Wc/Ni-Based Coating Remelting Study on Q235 Steel Surface. *Coatings* **2024**, *14*, 1172. [CrossRef]
11. Lee, C.; Park, H.; Yoo, J.; Lee, C.; Woo, W.; Park, S. Residual stress and crack initiation in laser clad composite layer with Co-based alloy and WC+ NiCr. *Appl. Surf. Sci.* **2015**, *345*, 286–294. [CrossRef]
12. Brückner, F.; Lepski, D.; Beyer, E. Modeling the influence of process parameters and additional heat sources on residual stresses in laser cladding. *J. Therm. Spray Technol.* **2007**, *16*, 355–373. [CrossRef]
13. Yu, Z.; Li, L.; Zhang, D.; Shi, G.; Yang, G.; Xu, Z.; Zhang, Z. Study of cracking mechanism and wear resistance in laser cladding coating of Ni-based alloy. *Chin. J. Mech. Eng.* **2021**, *34*, 92. [CrossRef]
14. Cao, Y.; Yan, K.; Shi, W.; Zhou, R.; Li, B.; Qin, J. Experimental Study on the Microstructure and Tribological Properties of Laser-Clad Ni60-WC Composite Coatings. *Materials* **2024**, *17*, 4638. [CrossRef]
15. Wang, H.; Liu, K.; Li, J.; Geng, S.; Jing, L.; Skuratov, V. Reinforcements/matrix micro-interface evolution and properties of in-situ Ni60A/WC coatings prepared by laser cladding. *Surf. Coat. Technol.* **2024**, *484*, 130834. [CrossRef]
16. Chen, H.; Lu, Y.; Wu, K.; Wang, X.; Liu, D. Effect of WC addition on TiC reinforced Fe matrix composites produced by laser deposition. *Surf. Coat. Technol.* **2022**, *434*, 128185. [CrossRef]
17. Ning, J.; Lan, Q.; Zhu, L.; Xu, L.; Yang, Z.; Xu, P.; Xin, B. Microstructure and mechanical properties of SiC-reinforced Inconel 718 composites fabricated by laser cladding. *Surf. Coat. Technol.* **2023**, *463*, 129514. [CrossRef]
18. Zhou, J.; Huang, Y.; Cai, Z.; He, G.; Xu, K.; Chen, Y.; Wang, H. Preparation of NiCrBSi-WC/Co coatings by stable magnetic field assisted supersonic plasma spraying and its wear resistance mechanism. *Mater. Charact.* **2022**, *194*, 112433. [CrossRef]
19. Meng, L.; Zhu, B.; Liu, X.; Zeng, X. Investigation on the Ni60-WC composite coatings deposited by extreme-high-speed laser-induction hybrid cladding technology: Forming characteristics, microstructure and wear behaviors. *Surf. Coat. Technol.* **2023**, *473*, 130033. [CrossRef]
20. Mahmood, T.; Mian, A.; Amin, M.R.; Auner, G.; Witte, R.; Herfurth, H.; Newaz, G. Finite element modeling of transmission laser microjoining process. *J. Mater. Process. Technol.* **2007**, *186*, 37–44. [CrossRef]
21. Heng, W.; Pang, M. Microstructure and wear resistance of laser cladding NiCrAlY/TC4 composite coatings with in-situ synthesized transition layer by modulating thermal boundary in nitrogen atmosphere. *J. Mater. Sci.* **2023**, *58*, 16119–16143. [CrossRef]
22. Zhang, Y.; Zhang, W.; Wang, L.; Xiao, T.; Meng, X.; Zhang, Z. Mechanism of the high-speed and long-run-out landslide considering the evolution of the frictional heat in the sliding zone. *Nat. Hazards* **2024**, *120*, 3299–3317. [CrossRef]
23. Liang, W.; Yang, Y.; Qi, K.; Jin, K.; Xiong, L. Quality evaluation of multi-path laser cladding coatings based on integrated fuzzy comprehensive evaluation and improved analytical hierarchy process method. *Surf. Coat. Technol.* **2021**, *427*, 127816. [CrossRef]
24. Du, Z.; Hu, Z.; Feng, Y.; Mo, F. The Effect of Powder Composition on the Microstructure and Corrosion Resistance of Laser Cladding 60NiTi Alloy Coatings on SS 316L. *Metals* **2021**, *11*, 1104. [CrossRef]
25. Wu, J.; Zhang, J.; Chen, D.; Huang, J.; Shi, W.; An, F.; Wu, X. Study on the Effect of CeO_2 on the Performance of WC + Ni60 Laser Cladding Coating. *Lubricants* **2025**, *13*, 24. [CrossRef]
26. Fan, H.; Yang, L.; Zhang, D.; Wu, H.; Yang, Y.; Wei, Z.; Liu, S. Enhancing epoxy coating corrosion resistance with a novel MoS2-modified polydopamine functionalized graphene oxide nanocomposite. *Colloids Surf. A Physicochem. Eng. Asp.* **2024**, *683*, 133080. [CrossRef]
27. Yu, S.; Sun, W.; Yong, H.; Yu, J.; Wu, Y.; Meng, Y. A variable diameter spiral path planning strategy for large eccentricity variable curvature rotating parts with focus on thickness and performance control in cladding. *Surf. Coat. Technol.* **2025**, *495*, 131487. [CrossRef]
28. Huang, D.; Xu, Z.; Jia, X.; Yu, H.; He, Y.; Dong, Z.; Zhang, H. Uniform microstructure and excellent corrosion resistance of HV0.2OF-Sprayed CoCrNi medium-entropy alloy coating in fluoride ion environment. *Met. Mater. Int.* **2024**, *30*, 61–76. [CrossRef]

29. He, X.; Kong, D.; Song, R. Microstructures and properties of laser cladding Al-TiC-CeO2 composite coatings. *Materials* **2018**, *11*, 198. [CrossRef]
30. Jiang, J.; Wang, B.; Yi, X.; Wang, Q.; Chen, W.; Ye, J. Probability-based horizontal fire spread scenarios in framed structures and data-driven prediction model. *J. Build. Eng.* **2025**, *101*, 111798. [CrossRef]

Disclaimer/Publisher's Note: The statements, opinions and data contained in all publications are solely those of the individual author(s) and contributor(s) and not of MDPI and/or the editor(s). MDPI and/or the editor(s) disclaim responsibility for any injury to people or property resulting from any ideas, methods, instructions or products referred to in the content.